Peak Broadening in Photoelectron Spectroscopy of Amorphous Polymers: the Leading Role of the Electrostatic Landscape

Laura Galleni,[*,†,‡] Arne Meulemans,[†] Faegheh S. Sajjadian,[†,‡] Dhirendra P. Singh,[‡] Shikhar Arvind,[†,‡] Kevin M. Dorney,[‡] Thierry Conard,[‡] Gabriele D'Avino,[¶] Geoffrey Pourtois,[‡] Daniel Escudero,[†] and Michiel J. van Setten[*,‡]

†Department of Chemistry, KU Leuven, Celestijnenlaan 200F, 3001 Leuven, Belgium

‡Imec, Kapeldreef 75, 3001 Leuven, Belgium

¶Grenoble Alpes University, CNRS, Grenoble INP, Institut Néel, 38042 Grenoble, France

E-mail: laura.galleni@imec.be; michiel.vansetten@imec.be

Abstract

The broadening in photoelectron spectra of polymers can be attributed to several factors, such as light source spread, spectrometer resolution, finite lifetime of the hole state, and solid-state effects. Here, for the first time, we set up a computational protocol to assess the peak broadening induced for both core and valence levels by solid-state effects in four amorphous polymers by using a combination of density functional theory, many-body perturbation theory, and classical polarizable embedding. We show that intrinsic local inhomogeneities in the electrostatic environment induce a Gaussian broadening of 0.2-0.7 eV in the binding energies of both core and semi-valence electrons, corresponding to a full width at half maximum (FWHM) of 0.5-1.7 eV for the investigated systems. The induced broadening is larger in acrylate- than in styrene-based polymers, revealing the crucial role of polar groups in controlling the roughness of the electrostatic landscape in the solid matrix.

TOC Graphic
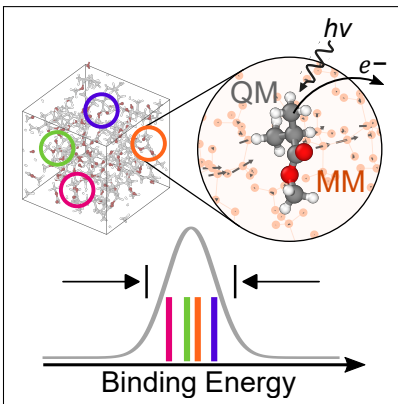
Photoelectron spectroscopy (PES) allows to study the composition of solids, liquids, and gaseous compounds by measuring the binding energies (BEs) of electrons in the material. In PES measurements, the electrons are extracted by the photoelectric effect using either x-rays (x-ray photoelectron spectroscopy, or XPS) or ultra-violet light (ultra-violet photoelectron spectroscopy, or UPS).[1] XPS is mostly used to probe the BEs of core-electrons, whereas UPS is used for valence- to semi-core-electrons. The interpretation of experimental XPS and UPS spectra is often complicated by the relatively large peak broadening, which tends to lead to overlapping peaks.

The peak broadening (ΔE) in PES of polymers originates from two types of sources:[2] (i) *extrinsic* sources, such as the light source spread and the spectrometer resolution (ΔE_{ext}), and (ii) *intrinsic* sources, such as the hole finite lifetime (ΔE_{τ}) and solid-state effects, such as disorder and inhomogeneities in the material (ΔE_{solid}). Assuming uncorrelated sources of Gaussian broadening, the total width is the convolution of all contributions:

$$\Delta E^2 = \Delta E_{ext}^2 + \Delta E_{\tau}^2 + \Delta E_{solid}^2 \tag{1}$$

Typically, the fitted values for the full width at half maximum (FWHM) of experimental spectra are in the range of 1.2-1.6 eV. The FWHM induced by extrinsic sources is generally in the range of 0.25-0.85 eV,[3,4] while the lifetime of a photohole is of the order of femtoseconds, which corresponds to an additional broadening of about 0.1-0.2 eV.[5,6]

Here, we propose a protocol based on first-principles calculations to estimate for the first time the contribution of solid-state effects to the broadening in XPS and UPS peaks of four common amorphous polymers: poly(methyl methacrylate) (PMMA), poly(t-butyl methacrylate) (PBMA), polystyrene (PS), and poly(4-hydroxystyrene) (PHS). These polymers were chosen as a test case for their vast range of applications[7,8] and in continuity with our previous work.[9]

An ideal model for theoretical PES spectra should yield the number of photoelectrons extracted from the sample as a function of their BEs. This requires three ingredients:

(i) the density of states (DOS), i.e., the distribution probability of electronic states as a function of their BEs; (ii) the photoionization cross-section, which is the probability of extracting an electron from an orbital given its BE and photon energy; and (iii) a model for kinetic energy loss due to the scattering of photoelectrons in their way out of the sample, which leads to an increasing background for larger BEs. Secondary effects such as satellite peaks are neglected here. Although (ii) and (iii) may be important to reach a quantitative interpretation of the experimental spectra, most of the information is already contained in the DOS. This is especially true for XPS spectra, where the photoionization cross-section is practically independent of the BEs[10] and the background can be easily subtracted using known expressions.[11] Therefore, in this work, we neglect (ii) and (iii) and focus on the simulation of the DOS, by calculating the electron BEs.

Several theoretical methods are available to calculate BEs. A first approximation consists in taking the Hartree-Fock energies with opposite sign, as stated in Koopman's theorem.[12] In the literature, Kohn-Sham energies from density functional theory (DFT) are also often considered, although these values are not physical as they represent the single-particle energy of the non-interacting auxiliary system. Another method to calculate binding energies is ΔSCF, where the BEs are calculated as the difference between the energy of the cation and that of the neutral system.[12,13] Many-body perturbation theory in its many flavours, such as the GW formalism,[14–17] are also often used. Previous works showed that GW yields very accurate valence and core-level BEs at an affordable computational cost.[18–23] However, the comparison with experiments requires introducing a peak broadening as a phenomenological parameter.

A popular technique to model amorphous solid materials is hybrid quantum mechanics/molecular mechanics (QM/MM).[24] In this approach, the atomic system is divided into two regions: a QM fragment which is modeled with a high-level quantum-mechanical technique, and the MM environment, which is described with a lower-level classical model. The combination of high- and low-level theories provides a good compromise between accuracy

4

and computational cost. A typical QM/MM scheme for the simulation of PES is the so-called electrostatic embedding.[24] In this scheme, the MM region is described with a classical polarizable model of atomistic resolution. Various works report BEs or ionization potentials calculated in a QM/MM framework with ΔSCF[25–29] or GW.[30–33] However, only few of these works focus on amorphous solids,[27,32] and although some attempts have been made on polymer chains,[28,33] only the work by Ehlert et al. reports calculated binding energies of a full amorphous model of a polymer,[27] although calculated only for core-levels using ΔSCF.

In this work, we improve on the results reported in the literature by (i) investigating four new polymer systems, (ii) considering amorphous atomistic models optimized at a higher level of theory, namely a combination of force-fields and DFT, and (iii) calculating both valence and core level binding energies using GW in the full-analytical approach,[17] which does not require the explicit creation of a hole, as opposed to ΔSCF, while allowing to treat core-electrons, in contrast to other implementations of GW such as contour-deformation or the plasmon-pole model used in similar works.[30–33] The electrostatic embedding scheme used in this work is illustrated in Figure 1.
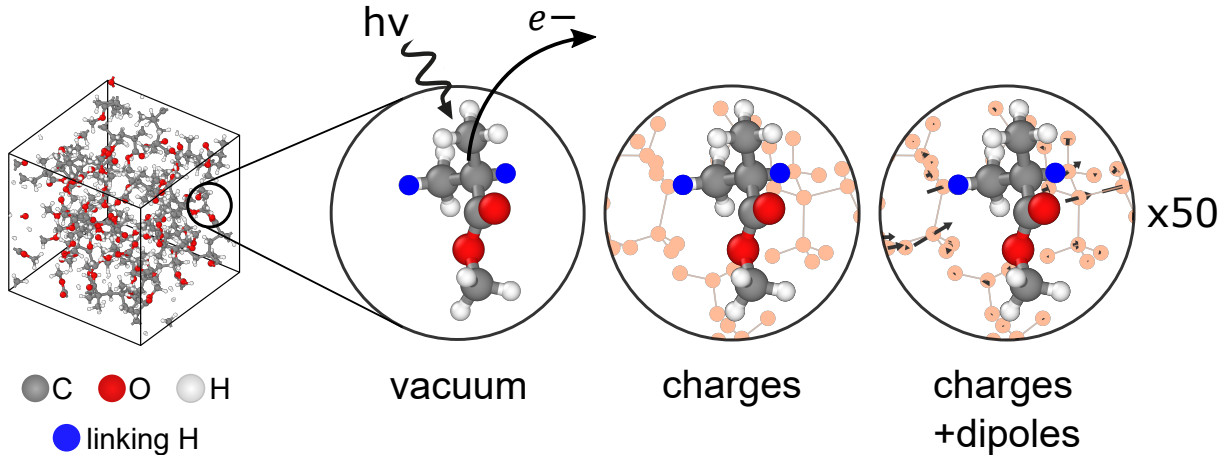

Figure 1: Scheme of the three approximations considered in this work: hydrogen-terminated repeat unit in vacuum, embedded in point charges, and embedded in point charges and dipoles. Calculations are repeated for 50 different repeat units of the polymer matrix.

To generate the atomic coordinates of each polymer structure, we follow a multi-step

protocol: first, a polymer of 50 repeat units is generated by means of our own polymer builder code, imposing a nominal density within $0.1 \, \mathrm{g \, cm^{-3}}$ from the experimental value (more details in the Supporting Information, SI); then, the structure is optimized by sequentially applying time-stamped force-bias Monte Carlo (TFMC)[34] and Broyden–Fletcher–Goldfarb–Shanno (BFGS) optimization[35] both using DFT forces and imposing periodic boundary conditions as implemented in the CP2K software package.[36]

Each one of the 50 repeat units of the polymer structure is then terminated with hydrogens and considered as the QM region for a separate QM/MM calculation to obtain the binding energies. The hydrogen-terminated repeat unit is henceforth called fragment. This choice of fragments has been justified for these particular polymers in a previous work[9] and is expected to be reasonable for most non-conjugated polymers where there is no significant delocalization of the electronic states. The BEs of each fragment are computed with single-shot GW (G_0W_0) in the fully-analytical approach[17] on top of DFT at the BH-LYP[37–39]/def2-TZVPP level of theory in combination with resolution of identity.[40–42] The MM atomistic environment corresponds to a cloud of about 200000 atomic charges and dipoles surrounding the QM region, obtained by replicating the simulation box in the three dimensions within a sphere of radius 80 Å, as to converge electrostatic potential. Fractional charges and induced dipoles in the neutral ground state are obtained from self-consistent microelectrostatic calculations (MESCal code)[43] for the neutral ground state of the entire simulation box, imposing periodic boundary conditions. MM embedding does not consider dynamical polarization effects arising from the reaction of the dielectric environment to the photo-hole, that, however, negligibly contribute to energetic disorder in bulk systems.[44] The intrinsic solid-state broadening is then estimated from the standard deviation of the BEs over the 50 fragments.

Figure 2 shows the BEs of the O 1s, C 1s and the upper 21 valence levels of 50 fragments of PMMA embedded in charges+dipoles. Similar figures for the other polymers are reported in the SI, Figures S1-S12. These Figures reveal significant fluctuations in the calculated BEs
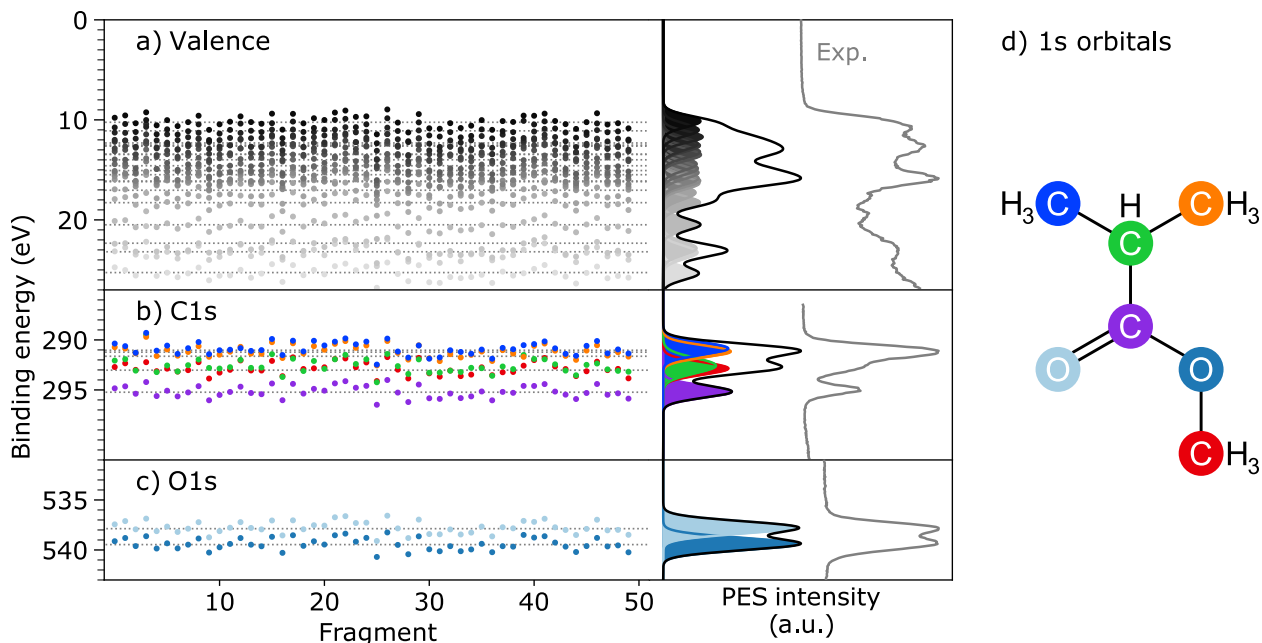
Figure 2: Distribution of the calculated binding energies for (a) valence, (b) C 1s, and (c) O 1s orbitals of 50 fragments of PMMA embedded in charges+dipoles, and (d) scheme of the corresponding C 1s and O 1s orbitals. Dotted lines in the left panel are the calculated values for the fragment relaxed in vacuum. Experimental XPS and UPS spectra of the polymer are normalized and aligned to the theory; the background is not subtracted.

for both core and valence levels, ultimately resulting in a sizeable peak broadening. Such an *energetic disorder* is a direct consequence of the roughness of the electrostatic landscape arising from the differences in the local environment of the 50 fragments, as confirmed by the correlations between BEs and the electrostatic potential, reported in the SI, Figure S13. The distribution of BEs appears symmetric around the average values, which in turn do not differ significantly from the values calculated on the isolated fragment relaxed in vacuum (dotted lines, see SI, Table S3). To simulate the spectra, we plot a Gaussian peak with width equal to the standard deviation over the 50 BEs, centered on the average values. The area of each Gaussian peak is normalized as we neglect here the contribution of the photo-ionization cross-section and assume that each orbital contributes equally to the photoelectron spectra. To justify the choice of a Gaussian line-shape, we perform a Shapiro-Wilk test [45] for each BE and find that only one peak out of 27 deviates from a normal distribution (see SI, Figure S16). The resulting theoretical DOS obtained from the sum of these Gaussian peaks

is in qualitative agreement with the experiment. Notice that no background was subtracted from the experimental data, which is why a discrepancy is visible at higher BEs. Moreover, a rigid shift to the calculated spectrum was applied to align the most intense peak to the experimental one, allowing a direct comparison of the relative peak positions. The shift, which is different for core and valence BEs and is in the range of 3-7 eV, accounts for several factors, such as the approximations involved in the computational scheme (incomplete basis set, DFT functional, GW self-energy), the different reference energies used in theory and experiment (vacuum and Fermi edge, respectively), and charging effects, as discussed in Ref.[9] Interestingly, the spread in energies is similar for both valence and core levels. This indicates that the electrostatic landscape varies over a length scale that is comparable to the molecular size, as confirmed by the analysis of the potential correlation function (see SI, Figure S15).

To ascertain that the spread is due to the local electrostatic environment and not to structural variations of the repeat units within the polymer, the calculation is repeated on each of the 50 fragments in vacuum without point charges and dipoles, as shown in Fig. 3a, bottom spectrum. Interestingly, the broadening induced by local geometrical variations is negligible with respect to the electrostatic effects, for both core and semi-valence orbitals. This result is in agreement with our previous work on 1s core level BEs[9] and is not surprising, as core-electron BEs are weakly sensitive to the position of the neighboring atoms due to the strong localization of the 1s orbitals. However, it is remarkable that the effect of geometry is negligible also for valence orbitals, where the stronger delocalization should, in principle, lead to a larger effect on the BEs. Moreover, the comparison between the charges and charges+dipoles embedding schemes show that the dipoles clearly contribute to the disorder, although their effect is smaller than that of charges alone.

To investigate the generality of these conclusions, the calculations were repeated on three additional polymers. The results are reported in Fig. 3b-d and Table 1. In all cases, the impact of structural variations is negligible, whereas the presence of charges and dipoles
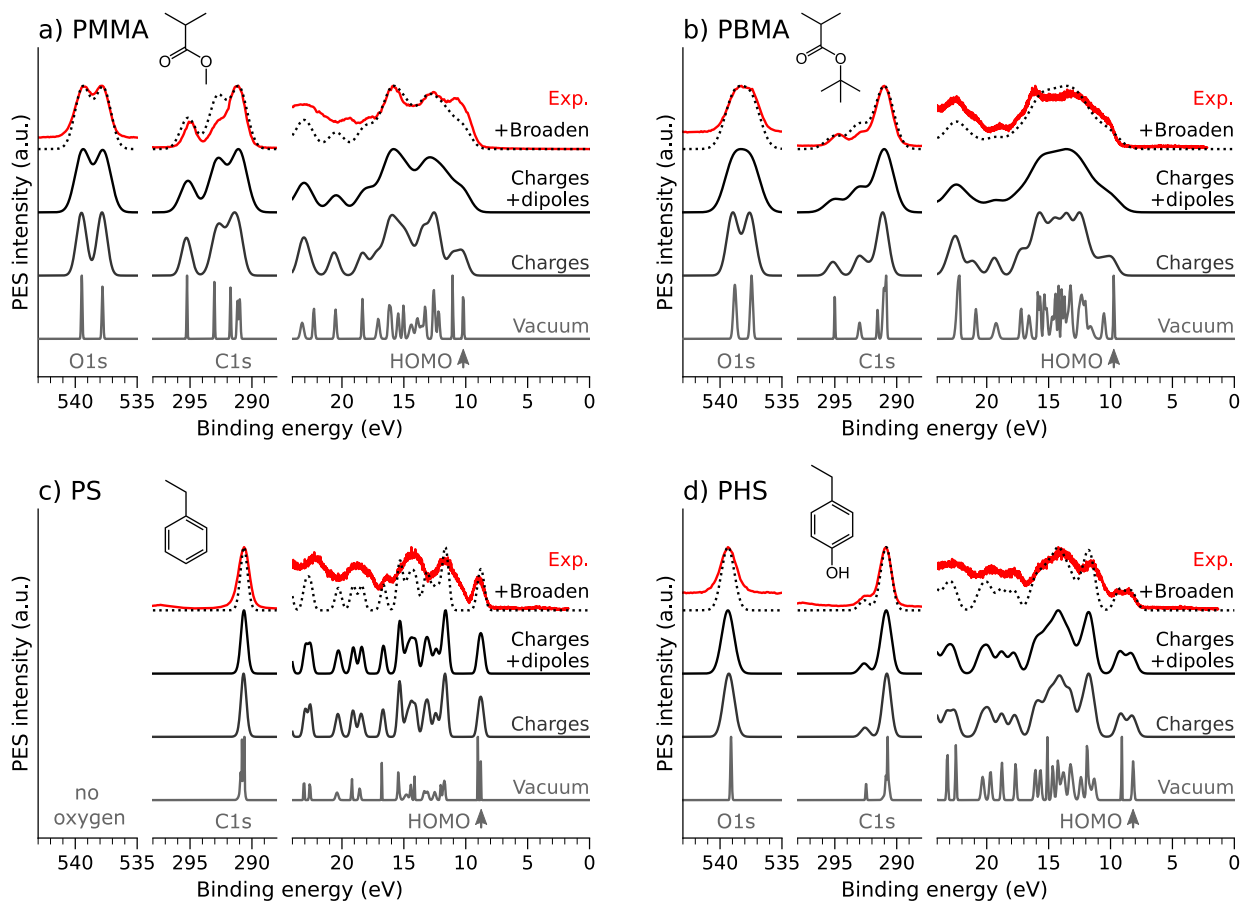
Figure 3: Experimental and calculated PES spectra for O 1s, C 1s, and valence regions of a) PMMA, b) PBMA, c) PS, and d) PHS in the three considered approximations and with the addition of a broadening of 0.3 eV to account for the finite lifetime and the instrumental resolution. Spectra are normalized and experimental data are aligned to the most intense theoretical peak in the charges+dipoles approximation, except for the UPS spectra of PBMA where the peak at 22.4 eV is considered instead.

Table 1: Average FWHM in eV calculated with G_0W_0 or DFT (parenthesis) over all O 1s, C 1s, and semi-valence BEs of 50 fragments.

ΔE_{solid} (eV)	PS	PHS	PMMA	PBMA
Vacuum	0.15 (0.09)	0.20 (0.13)	0.18 (0.15)	0.20 (0.19)
Charges	0.44 (0.39)	0.78 (0.74)	0.96 (0.96)	0.98 (0.97)
Charges + dipoles	0.49 (0.43)	0.91 (0.86)	1.48 (1.47)	1.68 (1.66)

9

induces a significant contribution to the peak broadening. Interestingly, the electrostatic spread depends on the type of polymer, being minimum in PS (0.49 eV) and maximum in PBMA (1.68 eV). Our calculations reveal a good correlation between the spread in BEs and the magnitude of the fragment dipole moments, see SI, Figure S14. This suggests that the energetic disorder is mostly originating from the dipole fields of the randomly oriented repeat units, hence being larger in systems with polar groups, such as hydroxyl and acrylate ones.

To verify that the calculated values for the solid-state broadening in polymers are compatible with the presence of additional sources of broadening, we add a FWHM of 0.3 eV to the theoretical spectra simulated in the charges+dipoles approximation to account for the lifetime broadening and the extrinsic sources, as shown in Fig. 3. The total broadening is calculated with Eq. 1, assuming $\Delta E_\tau = 0.2$ eV and $\Delta E_{ext} = 0.25$ eV which is the typical instrumental resolution for a monochromatized Al Kα light source.[4] The resulting spectra are reported in Fig. 3 and show an excellent agreement with experiments. It should be noted that our calculations describe the static component of the energetic disorder, neglecting the dynamical contribution associated with nuclear thermal motion. Therefore, the very good agreement with experiments suggests that the static component dominates over the dynamical one, as observed in other amorphous systems.[44] Nevertheless, the dynamical contribution may explain the small discrepancy observed in PS and PHS, where the simulated broadening is smaller than the experimental one.

Finally, we notice that the spread due to solid-state effects can be already retrieved at the DFT level (Table 1), showing that the effect of local electrostatic fluctuations is already captured by the Kohn-Sham energies. This result is not trivial and could not be assumed *a priori*. To reduce the computational cost, one could therefore estimate the peak broadening at the DFT level by sampling over different fragments in combination with electrostatic embedding. However, a G_0W_0 calculation is still needed to calculate the relative peak positions of the fragment, which cannot be accurately described with Kohn-Sham energies.

In conclusion, we have shown that a significant amount of broadening in photoelectron spectra of amorphous polymers arises from the effect of inhomogeneities in the local electrostatic landscape. First-principles calculations using a combination of many-body perturbation theory, density functional theory, and electrostatic embedding, show that the electrostatic variations alone lead to a FWHM of 0.5-1.7 eV, and that larger contributions are expected in polymers with acrylate groups (PMMA and PBMA) than in those containing only a phenol (PHS) or a phenyl group (PS). On the contrary, the broadening induced by local variations in the polymer geometry are negligible. The computational protocol proposed here can be potentially applied to other disordered materials to provide insights into the physics of the photoelectric processes.

Supporting information

Computational and experimental details; distribution of calculated BEs in vacuum, charges, and charges+dipoles for PMMA, PBMA, PHS, and PS; mean absolute deviation of the average BEs with respect to the BEs of the fragments in vacuum; fluctuations of the atomic potential, dipole of the repeat unit, correlation of the atomic potential; p-values of Shapiro tests.

References

(1) Suga, S.; Sekiyama, A. *Photoelectron Spectroscopy*; Springer, 2021.

(2) Bagus, P. S.; Ilton, E. S.; Nelin, C. J. The Interpretation of XPS Spectra: Insights Into Materials Properties. *Surf. Sci. Rep.* **2013**, *68*, 273–304.

(3) https://assets.thermofisher.com/TFS-Assets/CAD/Application-Notes/D16105.pdf, consulted on 24/08/2023.

(4) https://www.kratos.com/applications/techniques/x-ray-photoelectron-spectroscopy, consulted on 24/08/2023.

(5) Nicolas, C.; Miron, C. Lifetime Broadening of Core-Excited and-Ionized States. *J. Electron Spectrosc. Relat. Phenom.* **2012**, *185*, 267–272.

(6) Carroll, T.; Hahne, J.; Thomas, T.; Sæthre, L.; Berrah, N.; Bozek, J.; Kukk, E. Carbon 1s Core–Hole Lifetime in CO_2. *Phys. Rev. A* **2000**, *61*, 042503.

(7) Serrano-Aroca, Á.; Deb, S. *Acrylate Polymers for Advanced Applications*; IntechOpen, 2020.

(8) Scheirs, J.; Priddy, D. B. Modern Styrenic Polymers: Polystyrenes and Styrenic Copolymers. **2003**,

(9) Galleni, L.; Sajjadian, F. S.; Conard, T.; Escudero, D.; Pourtois, G.; van Setten, M. J. Modeling X-ray Photoelectron Spectroscopy of Macromolecules Using GW. *J. Phys. Chem. Lett.* **2022**, *13*, 8666–8672.

(10) Fadley, C. S.; Shirley, D. A. Electronic Densities of States From X-Ray Photoelectron Spectroscopy. *J. Res. Natl. Bur. Stand. A Phys. Chem.* **1970**, *74*, 543.

(11) Engelhard, M. H.; Baer, D. R.; Herrera-Gomez, A.; Sherwood, P. M. Introductory Guide to Backgrounds in XPS Spectra and Their Impact on Determining Peak Intensities. *J. Vac. Sci. Technol. A* **2020**, *38*, 063203.

(12) Viñes, F.; Sousa, C.; Illas, F. On the Prediction of Core Level Binding Energies in Molecules, Surfaces and Solids. *Phys. Chem. Chem. Phys.* **2018**, *20*, 8403–8410.

(13) Norman, P.; Dreuw, A. Simulating X-Ray Spectroscopies and Calculating Core-Excited States of Molecules. *Chem. Rev.* **2018**, *118*, 7208–7248.

(14) Aryasetiawan, F.; Gunnarsson, O. The GW Method. *Rep. Prog. Phys.* **1998**, *61*, 237–312.

(15) Onida, G.; Reining, L.; Rubio, A. Electronic Excitations: Density-Functional Versus Many-Body Green's-Function Approaches. *Rev. Mod. Phys.* **2002**, *74*, 601–659.

(16) Golze, D.; Dvorak, M.; Rinke, P. The GW Compendium: A Practical Guide to Theoretical Photoemission Spectroscopy. *Front. Chem.* **2019**, *7*, 377.

(17) van Setten, M. J.; Weigend, F.; Evers, F. The GW-Method for Quantum Chemistry Applications: Theory and Implementation. *J. Chem. Theory Comput.* **2013**, *9*, 232–246.

(18) van Setten, M. J.; Caruso, F.; Sharifzadeh, S.; Ren, X.; Scheffler, M.; Liu, F.; Lischner, J.; Lin, L.; Deslippe, J. R.; Louie, S. G. et al. GW 100: Benchmarking G_0W_0 for Molecular Systems. *J. Chem. Theory Comput.* **2015**, *11*, 5665–5687.

(19) Knight, J. W.; Wang, X.; Gallandi, L.; Dolgounitcheva, O.; Ren, X.; Ortiz, J. V.; Rinke, P.; Körzdörfer, T.; Marom, N. Accurate Ionization Potentials and Electron Affinities of Acceptor Molecules III: A Benchmark of GW Methods. *J. Chem. Theory Comput.* **2016**, *12*, 615–626.

(20) van Setten, M. J.; Costa, R.; Viñes, F.; Illas, F. Assessing GW Approaches for Predicting Core Level Binding Energies. *J. Chem. Theory Comput.* **2018**, *14*, 877–883.

(21) Golze, D.; Keller, L.; Rinke, P. Accurate Absolute and Relative Core-Level Binding Energies From GW. *J. Phys. Chem. Lett.* **2020**, *11*, 1840–1847.

(22) Li, J.; Jin, Y.; Rinke, P.; Yang, W.; Golze, D. Benchmark of GW Methods for Core-Level Binding Energies. *J. Chem. Theory Comput.* **2022**, *18*, 7570–7585.

(23) Mukatayev, I.; Sklénard, B.; Olevano, V.; Li, J. Electron Removal Energies in Noble-Gas Atoms up to 100 keV: Ab Initio *GW* Versus X-Ray Photoelectron Spectroscopy. *Phys. Rev. B* **2022**, *106*, L081125.

(24) Morzan, U. N.; Alonso de Armino, D. J.; Foglia, N. O.; Ramirez, F.; Gonzalez Lebrero, M. C.; Scherlis, D. A.; Estrin, D. A. Spectroscopy in Complex Environments From QM—MM Simulations. *Chem. Rev.* **2018**, *118*, 4071–4113.

(25) Niskanen, J.; Murugan, N. A.; Rinkevicius, Z.; Vahtras, O.; Li, C.; Monti, S.; Carravetta, V.; Ågren, H. Hybrid Density Functional–Molecular Mechanics Calculations for Core-Electron Binding Energies of Glycine in Water Solution. *Phys. Chem. Chem. Phys.* **2013**, *15*, 244–254.

(26) Löytynoja, T.; Niskanen, J.; Jänkälä, K.; Vahtras, O.; Rinkevicius, Z.; Ågren, H. Quantum Mechanics/Molecular Mechanics Modeling of Photoelectron Spectra: The Carbon 1s Core-–Electron Binding Energies of Ethanol—Water Solutions. *J. Phys. Chem. B* **2014**, *118*, 13217–13225.

(27) Ehlert, C.; Kroener, D.; Saalfrank, P. A Combined Quantum Chemical/Molecular Dynamics Study of X-Ray Photoelectron Spectra of Polyvinyl Alcohol Using Oligomer Models. *J. Electron Spectros. Relat. Phenomena* **2015**, *199*, 38–45.

(28) Löytynoja, T.; Harczuk, I.; Jänkälä, K.; Vahtras, O.; Ågren, H. Quantum-Classical Calculations of X-Ray Photoelectron Spectra of Polymers—Polymethyl Methacrylate Revisited. *J. Chem. Phys.* **2017**, *146*, 124902.

(29) Ge, G.; Zhang, J.-R.; Wang, S.-Y.; Wei, M.; Hua, W. A QM/MM Study on the X-ray Spectra of Organic Proton Transfer Crystals of Isonicotinamides. *J. Phys. Chem. C* **2022**, *126*, 15849–15863.

(30) Li, J.; D'avino, G.; Duchemin, I.; Beljonne, D.; Blase, X. Combining the Many-Body GW Formalism With Classical Polarizable Models: Insights on the Electronic Structure of Molecular Solids. *J. Phys. Chem. Lett.* **2016**, *7*, 2814–2820.

(31) Li, J.; D'Avino, G.; Duchemin, I.; Beljonne, D.; Blase, X. Accurate Description of Charged Excitations in Molecular Solids From Embedded Many-Body Perturbation Theory. *Phys. Rev. B* **2018**, *97*, 035108.

(32) Tirimbò, G.; de Vries, X.; Weijtens, C. H.; Bobbert, P. A.; Neumann, T.; Coehoorn, R.; Baumeier, B. Quantitative predictions of photoelectron spectra in amorphous molecular solids from multiscale quasiparticle embedding. *Phys. Rev. B* **2020**, *101*, 035402.

(33) Tirimbò, G.; Sundaram, V.; Çaylak, O.; Scharpach, W.; Sijen, J.; Junghans, C.; Brown, J.; Ruiz, F. Z.; Renaud, N.; Wehner, J. et al. Excited-state electronic structure of molecules using many-body Green's functions: Quasiparticles and electron–hole excitations with VOTCA-XTP. *J. Chem. Phys.* **2020**, *152*.

(34) Mees, M. J.; Pourtois, G.; Neyts, E. C.; Thijsse, B. J.; Stesmans, A. Uniform-Acceptance Force-Bias Monte Carlo Method With Time Scale To Study Solid-State Diffusion. *Phys. Rev. B* **2012**, *85*, 134301.

(35) Broyden, C. G. The Convergence of a Class of Double-rank Minimization Algorithms 1. General Considerations. *IMA J. Appl. Math.* **1970**, *6*, 76–90.

(36) Kühne, T. D.; Iannuzzi, M.; Ben, M. D.; Rybkin, V. V.; Seewald, P.; Stein, F.; Laino, T.; Khaliullin, R. Z.; Schütt, O.; Schiffmann, F. et al. CP2K: An Electronic Structure and Molecular Dynamics Software Package – Quickstep: Efficient and Accurate Electronic Structure Calculations. *J. Chem. Phys.* **2020**, *152*, 194103.

(37) Becke, A. D. Density-Functional Exchange-Energy Approximation With Correct Asymptotic Behavior. *Phys. Rev. A* **1988**, *38*, 3098–3100.

(38) Lee, C.; Yang, W.; Parr, R. G. Development of the Colle-Salvetti Correlation-Energy Formula Into a Functional of the Electron Density. *Phys. Rev. B* **1988**, *37*, 785–789.

(39) Becke, A. D. A New Mixing of Hartree–Fock and Local Density-Functional Theories. *J. Chem. Phys.* **1993**, *98*, 1372–1377.

(40) Eichkorn, K.; Treutler, O.; Öhm, H.; Häser, M.; Ahlrichs, R. Auxiliary Basis Sets To Approximate Coulomb Potentials. *Chem. Phys. Lett.* **1995**, *240*, 283–290.

(41) Weigend, F.; Ahlrichs, R. Balanced Basis Sets of Split Valence, Triple Zeta Valence and Quadruple Zeta Valence Quality for H to Rn: Design and Assessment of Accuracy. *Phys. Chem. Chem. Phys.* **2005**, *7*, 3297–3305.

(42) Weigend, F. Accurate Coulomb-Fitting Basis Sets for H to Rn. *Phys. Chem. Chem. Phys.* **2006**, *8*, 1057–1065.

(43) D'Avino, G.; Muccioli, L.; Zannoni, C.; Beljonne, D.; Soos, Z. G. Electronic Polarization in Organic Crystals: A Comparative Study of Induced Dipoles and Intramolecular Charge Redistribution Schemes. *J. Chem. Theory Comput.* **2014**, *10*, 4959–4971.

(44) D'Avino, G.; Muccioli, L.; Castet, F.; Poelking, C.; Andrienko, D.; Soos, Z. G.; Cornil, J.; Beljonne, D. Electrostatic Phenomena in Organic Semiconductors: Fundamentals and Implications for Photovoltaics. *J. Phys. Condens. Matter* **2016**, *28*, 433002.

(45) Shapiro, S. S.; Wilk, M. B. An Analysis of Variance Test for Normality (Complete Samples). *Biometrika* **1965**, *52*, 591–611.

SUPPLEMENTARY INFORMATION

Peak Broadening in Photoelectron Spectroscopy of Amorphous Polymers: the Leading Role of the Electrostatic Landscape

Laura Galleni,[*,†,‡] Arne Meulemans,[†] Faegheh S. Sajjadian,[†,‡] Dhirendra P. Singh,[‡] Shikhar Arvind,[†,‡] Kevin M. Dorney,[‡] Thierry Conard,[‡] Gabriele D'Avino,[¶] Geoffrey Pourtois,[‡] Daniel Escudero,[†] and Michiel J. van Setten[‡]

[†]Department of Chemistry, KU Leuven, Celestijnenlaan 200F, 3001 Leuven, Belgium

[‡]Imec, Kapeldreef 75, 3001 Leuven, Belgium

[¶]Grenoble Alpes University, CNRS, Grenoble INP, Institut Néel, 38042 Grenoble, France

E-mail: laura.galleni@imec.be

Computational details

The initial guess of the atomistic structure of each polymer was generated by means of a coarse-grained molecular dynamics algorithm, implemented in our own polymer builder python code. The algorithm allows to generate polymer chains within a box of fixed volume with periodic boundary conditions. The atomistic structure of each repeat unit is first converted into a bead, consisting of a collection of rigid spheres, to decrease the degrees of freedom and to reduce the computational cost. Then the beads are distributed in random positions within the box. As a following step, a molecular dynamics simulation is carried out, where the beads interact through a Lennard-Jones potential, as well as attractive and repulsive forces applied locally at the backbone atoms of each repeat unit, until bonds are formed between the backbone atoms of different beads. At the end of the simulation, the beads are reverse-mapped into atoms and hydrogens are added as endcaps at the end of each polymer chain along the backbone direction, at a distance of 1.09 Å from the nearest backbone atom. The algorithm allows to achieve a high polymer entanglement and gives control over the total number of repeating units and the density, whereas the degree of polymerisation is the result of the simulation and it can be partially controlled by tuning the simulation parameters.

The most relevant parameters for the generation of the polymer structures are reported in Table S1. In this work we limit the number of repeat units in each structure to 50, corresponding to 750-1200 atoms depending on the type of polymer, in order to ensure the computational feasibility of the following optimization step with higher-level methods. The box size is chosen to simulate the experimental density within 0.1 g cm^{-3} from the experimental values.[1] The number of polymer chains in each structure ranges between 3 and 4, with a degree of polymerisation between 3 and 38 repeat units.

Table S1: Details of the four polymer structures considered in this work.

	PS	PHS	PMMA	PBMA
n. atoms	800	850	750	1200
box size (Å)	20.525	21.527	19.062	22.770
density (g cm^{-3})	1.0	1.0	1.2	1.0
chains (n. repeat units)	4, 8, 38	3, 9, 12, 26	9, 19, 22	5, 10, 35
n. hydrogen caps	6	8	2	4

The polymer structures were then optimized by sequentially applying time-stamped force-bias Monte Carlo (TFMC)[2] and Broyden–Fletcher–Goldfarb–Shanno (BFGS) optimization[3] both using DFT forces and imposing periodic boundary conditions as implemented in the CP2K software package.[4] Due to the periodic boundary conditions, some repeat units inevitably lie at the boundary of the box. As this can cause problems in the electrostatic embedding step calculation, the repeat units at the edge of the box are unfolded along the

box edges. Then, the unfolded polymer structure is replicated in the three directions within a cutoff of 80 Å, resulting in a total of about 200,000 atomic locations.

For the MM region, atomic charges and induced dipole moments are then computed at each atomic location of the replicated structure, excluding the hydrogen terminations at the chain ends, where no charge is assigned. Fractional charges and dipole moments are then calculated self-consistently on the replicated atomic coordinates using the micro-electrostatic scheme implemented in the MESCal code,[5] starting from electrostatic potential (ESP) charges and the polarizability tensor calculated with Turbomole 7.2[6] using DFT at the BH-LYP[7–9]/def2-TZVPP[10–12] level of theory on the isolated hydrogen-terminated repeat unit optimized with PBE[13]/def2-TZVP[11] in vacuum. The ESP charges of each of the two hydrogen terminations were redistributed to the neighboring carbon atoms to ensure a one-to-one charge mapping to the atoms of the repeat units in the polymer chains in the MESCal calculation. In the MESCal calculation, the intermolecular dipolar fields were screened imposing a screening parameter of 3 Å to avoid overpolarization between close atoms. Moreover, a uniform depolarization field was added to counterbalance the spurious polarization field induced by the residual total dipole, which is non-zero due to the finite system size.

For the QM region, each of the 50 repeat units of the central polymer box was considered for a separate QM-MM calculation. Hydrogen atoms were added to the QM repeat unit at a fixed bond distance of 1.09 Å along the direction of the C-C bond to the neighboring repeat units in the chain. Then, the electron binding energies of the QM hydrogen-terminated repeat unit (henceforth called fragment) were calculated with Turbomole 7.2[6] using G_0W_0[14] on top of a self-consistent field DFT calculation. The DFT calculation was performed using the BH-LYP[7–9] functional and a Gaussian basis set of triple-ζ valence plus polarization quality (def2-TZVPP) in combination with resolution of identity.[10–12] The dielectric function was computed in the Random-Phase Approximation (RPA) including all excitations.[14] The frequency dependence of the self-energy was treated with a fully analytical approach and the quasi-particle equations were solved by linearization.[14] The calculations were repeated in three conditions: (i) fragment in vacuum, (ii) fragment embedded in ESP atomic charges, and (iii) fragment embedded in ESP atomic charges and induced atomic dipoles. For the embedding calculations, we considered the charges and dipoles of the full replicated structure within a cutoff of 80 Å, and attention was paid to remove the charges and dipoles located on the atoms of the QM fragment. Dipoles were converted into pairs of point charges at a dipole distance of 0.001 Å and added to the Turbomole *control* file as two separate point charges.

The electrostatic broadening was then estimated as the standard deviation of the binding energies over the 50 fragments.

Experimental methods

PMMA

PMMA (Allresist AR-P 672.01, M_w = 950 kDa) was spin-coated on a 200 mm Si wafer at 1300 rpm for 30 s followed by soft-bake at 150°C for 180 s. The nominal film thickness post bake was ~40 nm as measured by ellipsometry. The model used for ellipsometry was Cauchy Layer/Silicon(substrate). The wafer was then diced into 3 cm × 3 cm coupons for further analysis. The XPS measurements were carried out in Angle Integrated mode using a QUANTES instrument from Physical electronics. The measurements were performed using a monochromatized photon beam of 1486.6 eV at an exit angle of 45 degree. A 100 μm^2 X-ray spot and a pass energy of 55 eV were used, leading to a energy resolution of ~ 0.7 eV as measured on the Ag 3d5/2 transition. Dual beam charge neutralization was used during this experiment.

The valence band photoelectron spectrum (PES) of PMMA was measured using an experimental setup comprised of two sub-systems; a Hemispherical photoelectron analyzer KREIOS 150 (SPECS GmbH) coupled with a laser-driven EUV light source (XUUS4 KM Labs) based on high-harmonic generation (HHG). The HHG process was performed in Argon gas, resulting a tunable spectrum with a bright, narrowband harmonic at ~ 42 eV ($\Delta\lambda/\lambda \sim 10^{-2}$) that was used in this work. The 42 eV EUV beam was coupled into the KREIOS spectrometer via a toroidal focusing mirror ($f = 40$ cm) resulting in a spot size of about 100×50 μm^2 (elongated due to a grazing incidence angle of ~30 degrees). Samples of PMMA coated on a Si wafer of the same composition and film thickness as used in the XPS measurements were mounted on a metal plate with a conducting clip to minimize effects of surface charging and transferred into the analysis chamber ($\sim 5 \times 10^{-10}$ mbar) of the KREIOS tool for PES measurements. The incident EUV beam power was attenuated using aluminum foils placed upstream in the beamline to further reduce effects of surface charging and to ensure no degradation of the PMMA occurred during the measurement. The PES spectra were collected with a pass energy of 100 eV and the entrance slit set to 0.8 mm at the entrance of the hemispherical analyzer.

PBMA, PS, and PHS

Solutions of 0.5 wt% of PBMA and PS in toluene and PHS in propylene glycol methyl ether acetate (PGMEA) were spin-coated on 2 cm × 2 cm silicon coupons in a cleanroom environment, with approximate thicknesses of 24, 21 and 15 nm respectively. The obtained films were then submitted to a post application bake at 100°C for 60 s.

The XPS and UPS measurements were performed in a VersaProbe III instrument from Ulvac-PHI using X-ray and UV photon beams from a monochromatized Al Kα (1486.6 eV) and a He II (40.8 eV) from a helium discharge lamp, respectively. Prior to each measurement, the samples were kept in the vacuum chamber for one night to ensure that all material

outgassing was complete and that the vacuum level in the chamber was sufficiently low (in the range of 10^{-8} Pa).

In XPS measurements, to minimize possible degradation due to X-rays, the measurement time was limited to about 3 minutes per spectrum and a large exposure spot size of 1000 μm $\times$500 μm was used.[15] All spectra were recorded at a take-off angle of 45°.

For UPS measurements, a negative bias of 5 V was applied to the sample holder and spectra were recorded at a take-off angle of 90°. Also due to high photon flux from He II source, intense charging effect happens on the samples. Therefore, an electron flood gun which provided low energy electrons of 1 to 2 eV, was used to compensate the charging. This energy is lower than 4 eV, which is the cut-off energy leading to chemical modification of the samples. In order to minimize possible degradation due to UV photons, the measurement time was limited to about 4 minutes per spectrum.

Calculated binding energies

The following plots depict the calculated binding energies of (a) valence, (b) C 1s, and (c) O 1s orbitals for PMMA, PBMA, PS and PHS. For each polymer, binding energies were calculated over 50 fragments in (i) vacuum, (ii) charges, and (iii) charges+dipoles. Dotted lines are the calculated values for the fragment in vacuum on the geometry optimized with DFT at the PBE[13]/def2-TZVP[11] level of theory. Gaussian peaks are area-normalized, centered on the average binding energies and with width equal to the standard deviation. The intensity of the theoretical spectra (black) obtained by the sum of the Gaussian peaks are normalized within each energy range.

PMMA
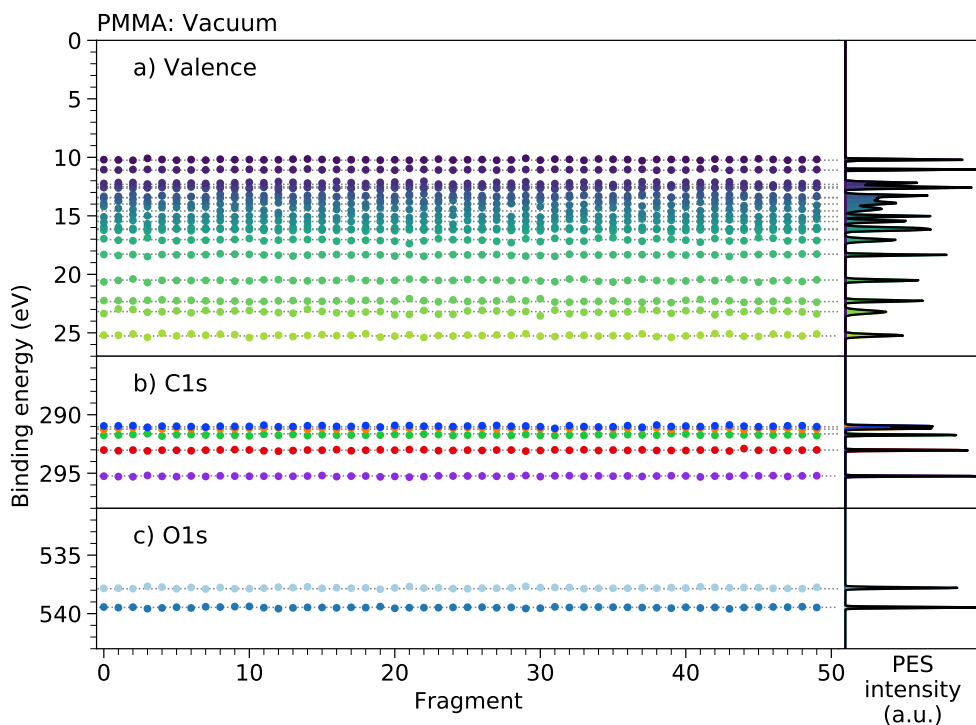
Figure S1
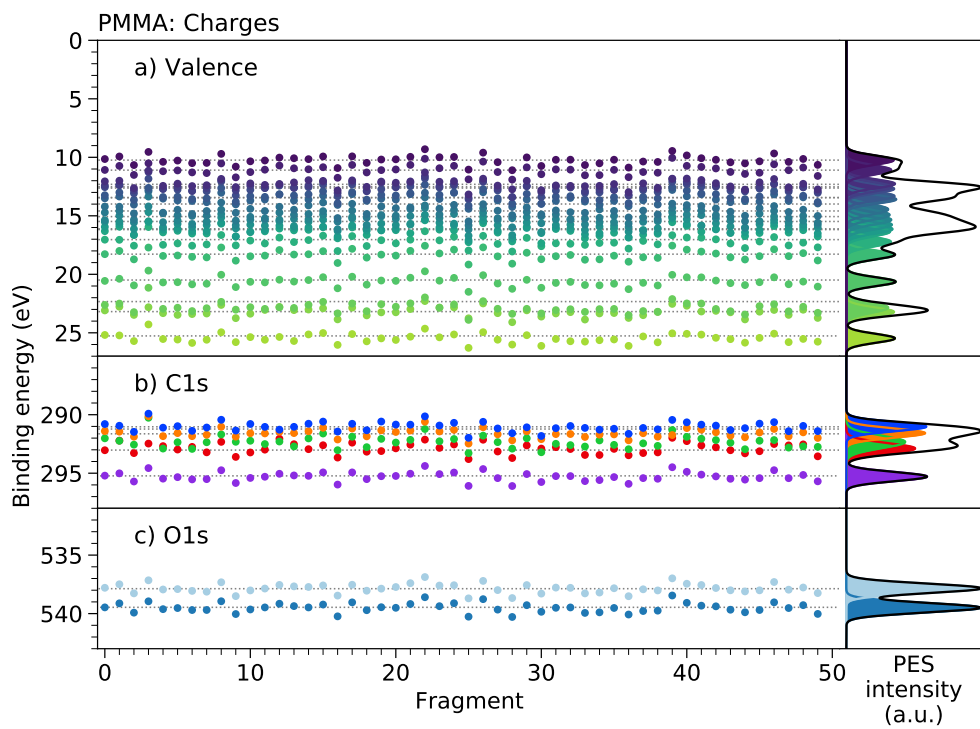
Figure S2
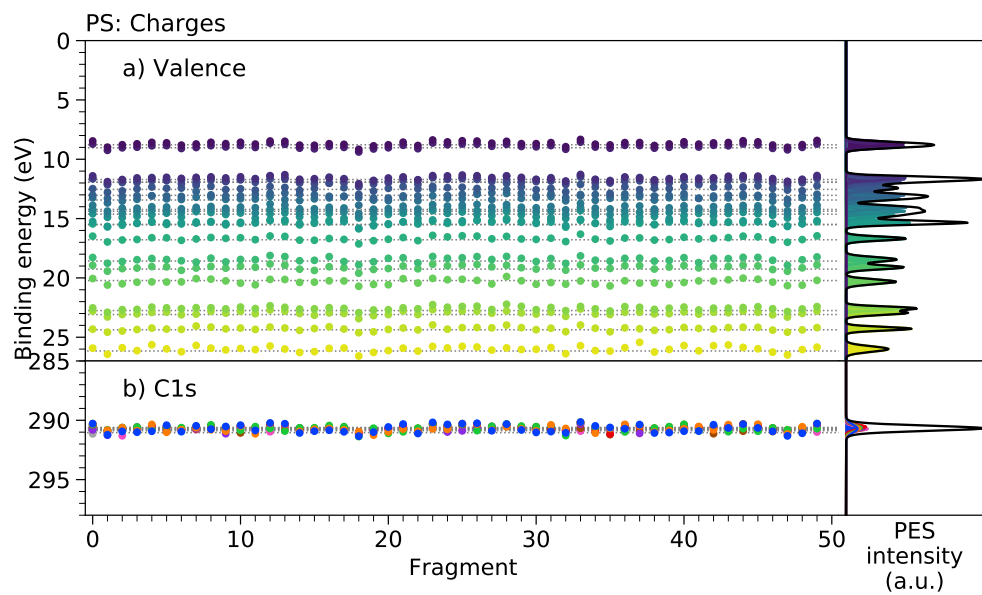

Figure S3

S-7
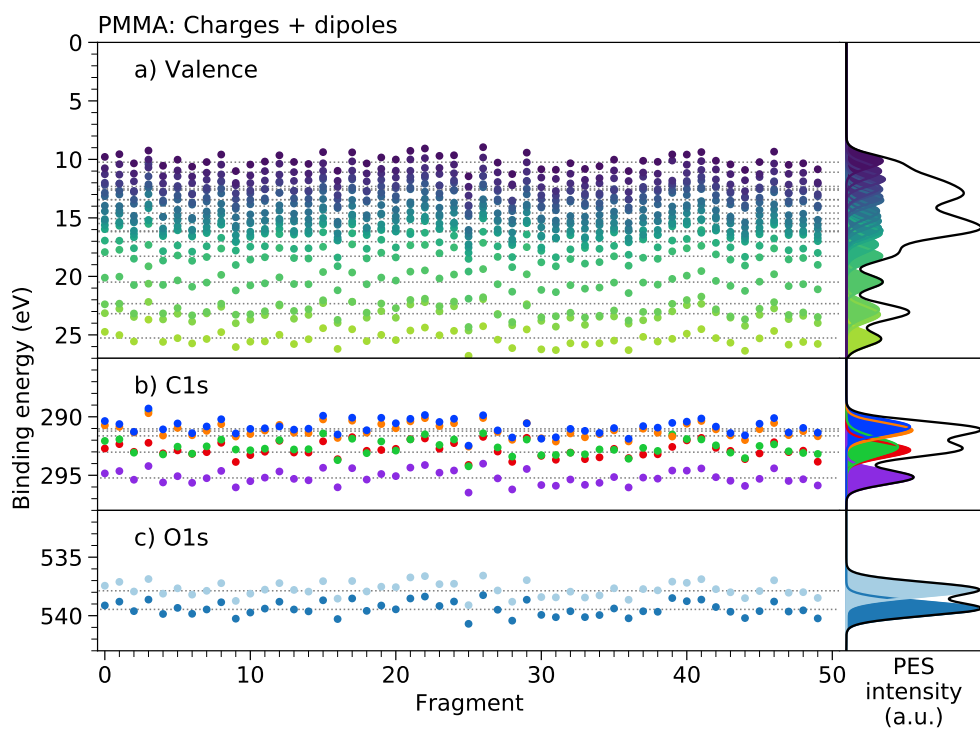
PBMA
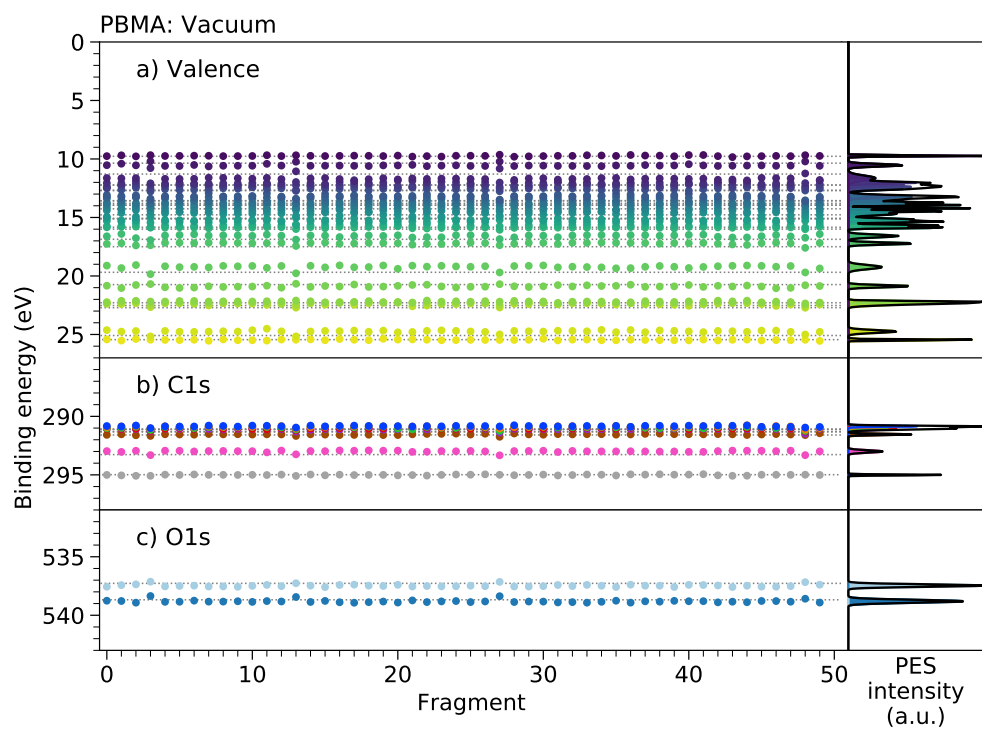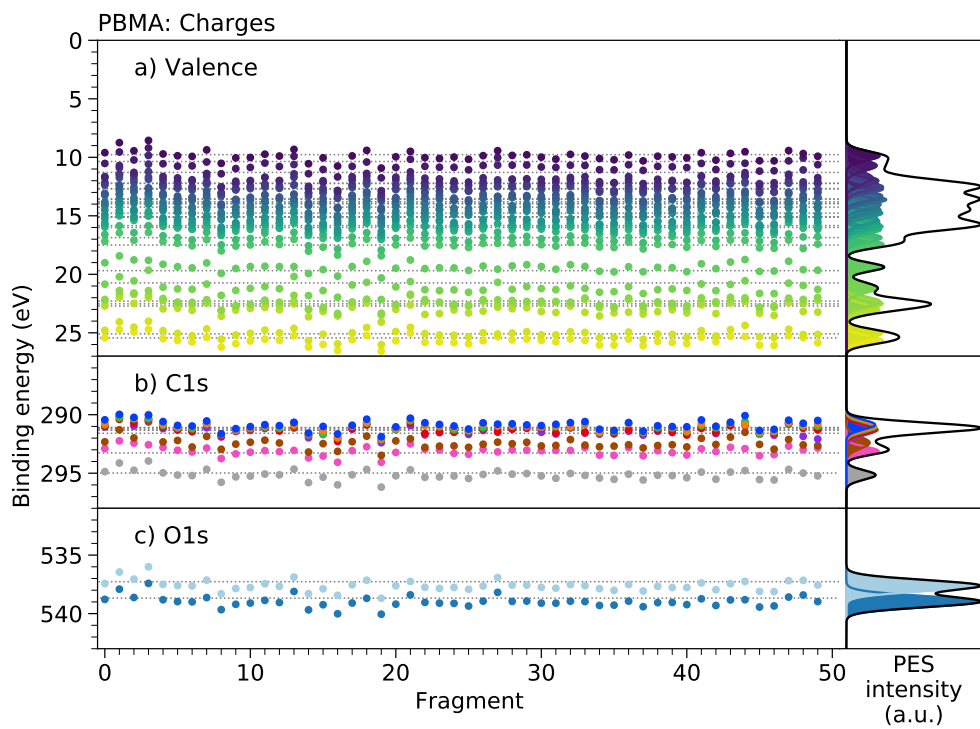
Figure S4

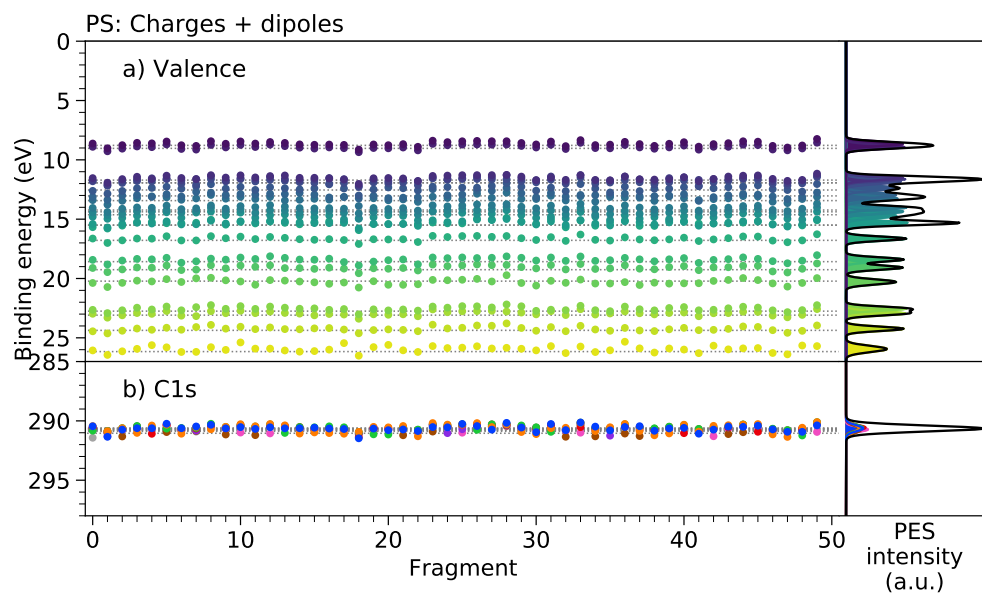Figure S5
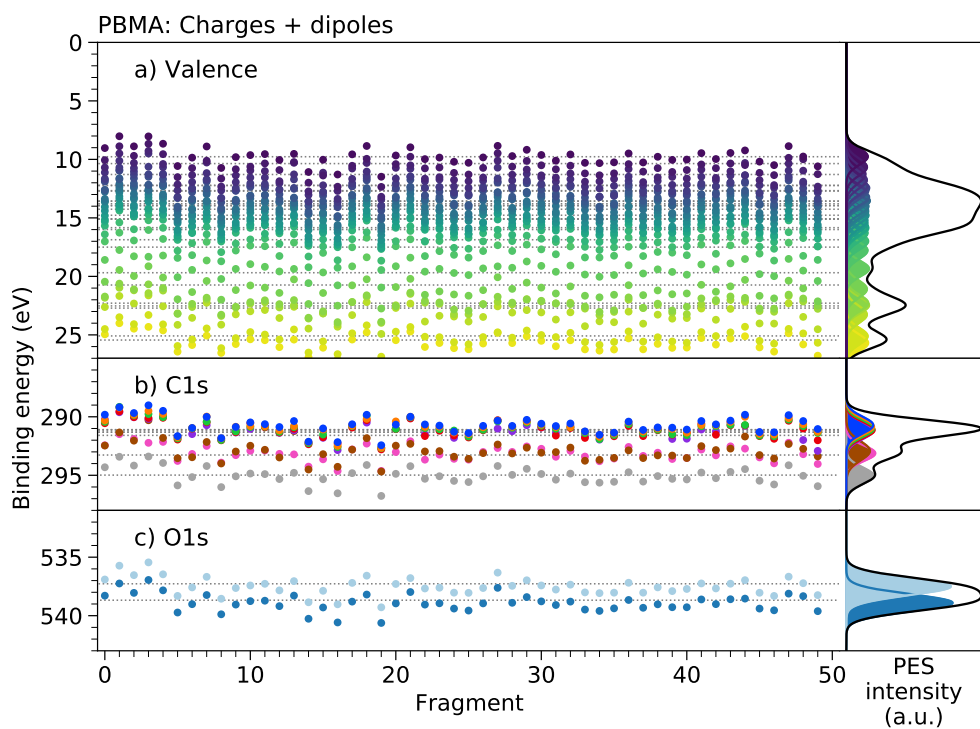
Figure S6

PS
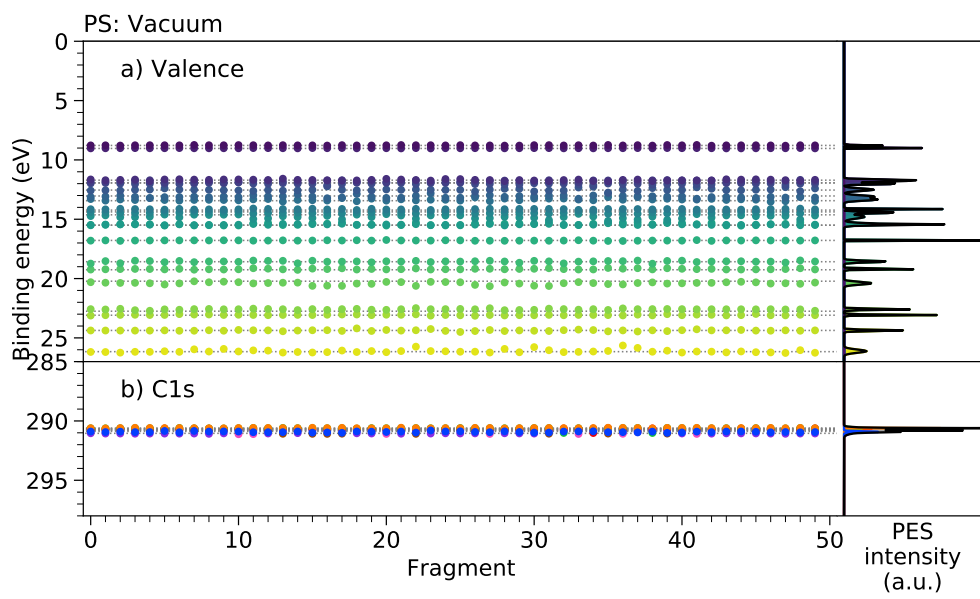
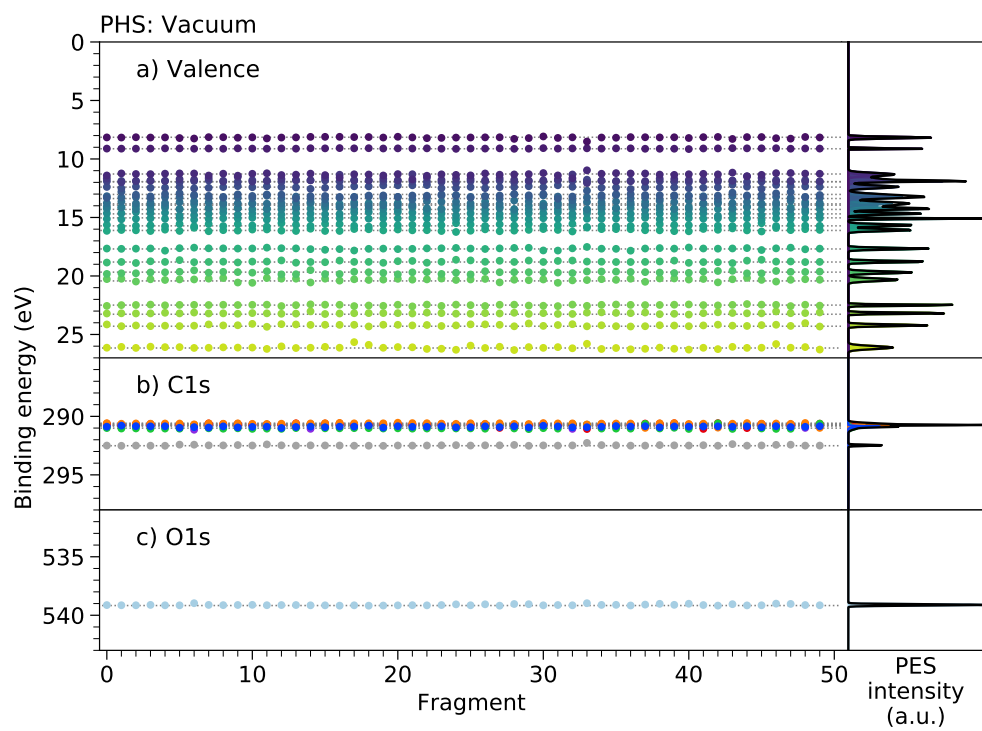
Figure S7

Figure S8

Figure S9
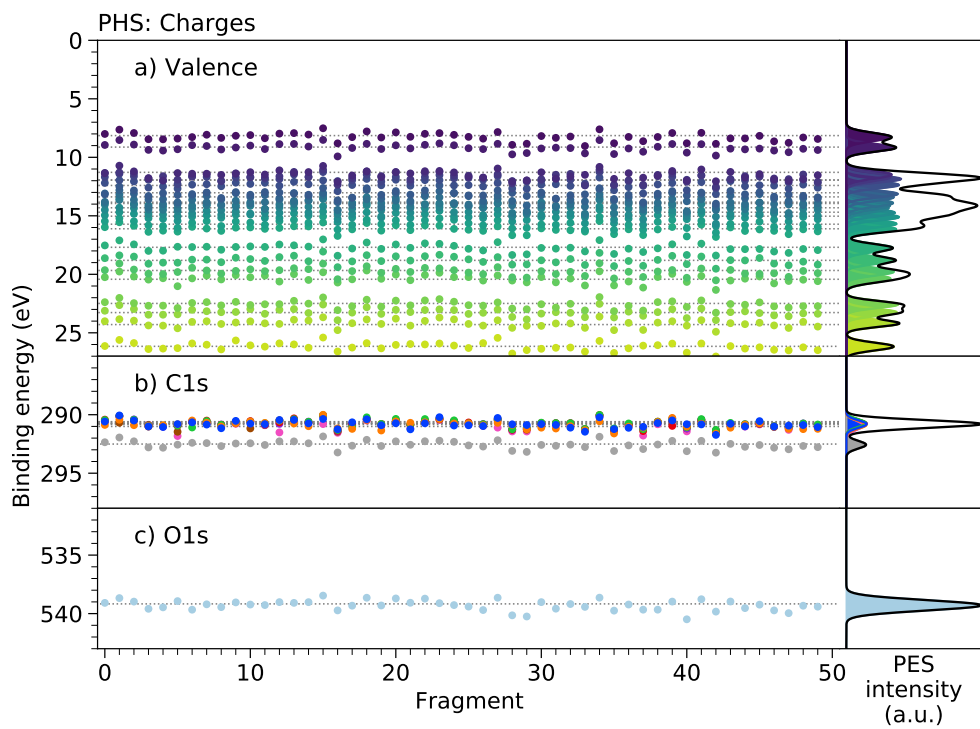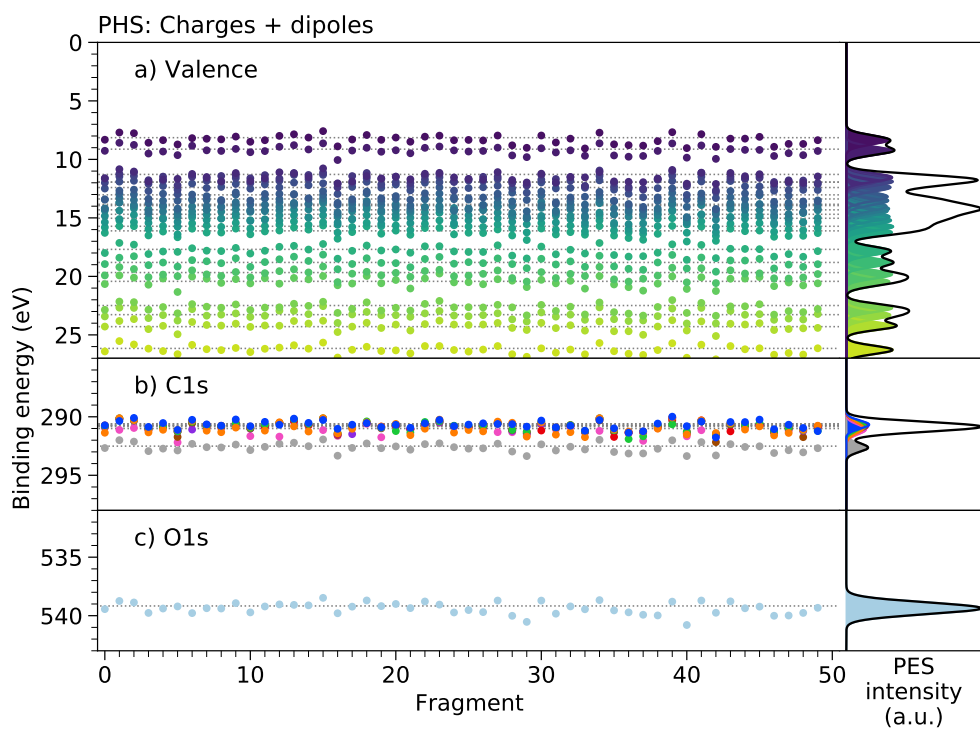
PHS

Figure S10

Figure S11

Figure S12

Average BEs: vacuum vs. MM embedding

Table S2: Mean absolute deviation in eV calculated with G_0W_0 or DFT (parenthesis) of the average BEs with respect to the BEs of the isolated fragments relaxed in vacuum.

	PS	PHS	PMMA	PBMA
Vacuum	0.06 (0.05)	0.05 (0.04)	0.06 (0.05)	0.20 (0.19)
Charges	0.11 (0.11)	0.08 (0.07)	0.17 (0.16)	0.21 (0.19)
Charges + dipoles	0.14 (0.13)	0.14 (0.12)	0.19 (0.18)	0.24 (0.22)

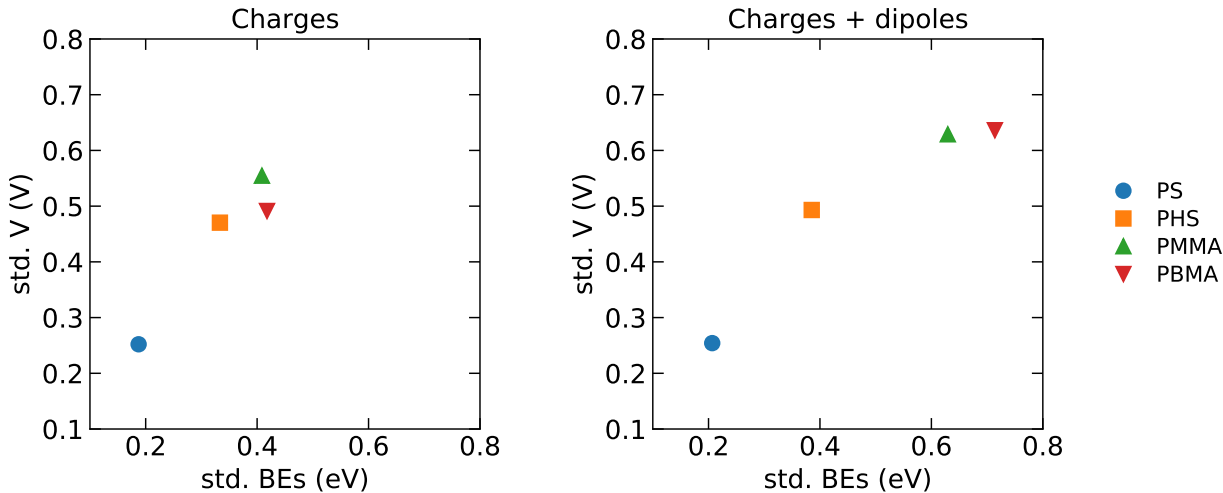# BE fluctuations vs. electrostatic disorder

Figure S13: Correlation between the fluctuations of the atomic potential (std. V, from classical microelectrostatic calculations) and the Gaussian peak broadening (std. BEs, from embedded *GW*) for charges (*left*), and charges+dipoles (*right*), for the four systems under study. The fluctuation of the atomic potential (std. V) is calculated as the standard deviation over all atomic sites. The Gaussian peak broadening (std. BEs) is calculated as the average, over all core and valence orbitals, of the standard deviation of the BEs over the 50 fragments, which is proportional to the FWHM values reported in Table 1. The correlations between the two quantities allows us to ascribe the fluctuation in BE to the roughness of the electrostatic disorder in the different samples.
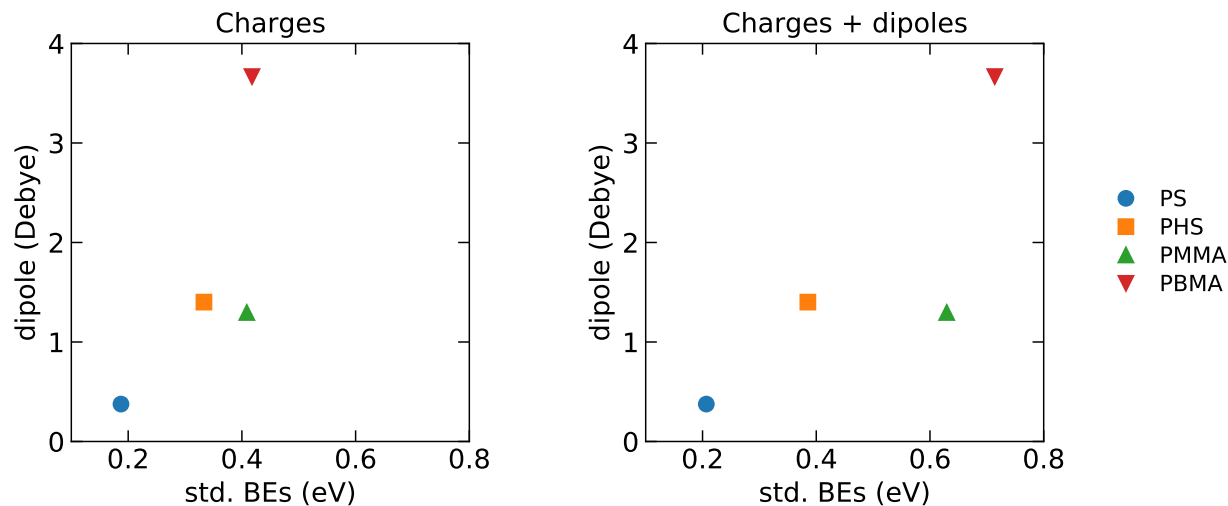
Repeat unit dipole vs. BE fluctuations

Figure S14: Correlation between the dipole of the hydrogen-terminated repeat unit and the Gaussian peak broadening for charges (*left*), and charges+dipoles (*right*), for the four systems under study. The dipole is calculated with Turbomole 7.2[6] using DFT at the BH-LYP[7–9]/def2-TZVPP[10–12] level of theory on the isolated hydrogen-terminated repeat unit optimized with PBE[13]/def2-TZVP[11] in vacuum. The Gaussian peak broadening (std. BEs) is calculated as the average, over all core and valence orbitals, of the standard deviation of the BEs over the 50 fragments, which is proportional to the FWHM values reported in Table 1. The correlation between the two quantities allows us to conclude that BE fluctuations originated from the electrostatic disorder caused by the randomly-oriented dipoles of the repeat units.

Spatial correlations of the electrostatic potential

The spatial correlation function of the electrostatic potential is calculated as:

$$C(r) = \frac{1}{\sigma^2} \langle \, (V(r_i) - \langle V(r_i) \rangle) \, (V(r_i + r) - \langle V(r_i) \rangle) \, \rangle \tag{S1}$$

where $V(r_i)$ is the electrostatic potential (from classical microelectrostatic calculations) at atom i and σ^2 is the variance of atomic potential fluctuations. Angle brackets indicate the average over the atoms in the sample.
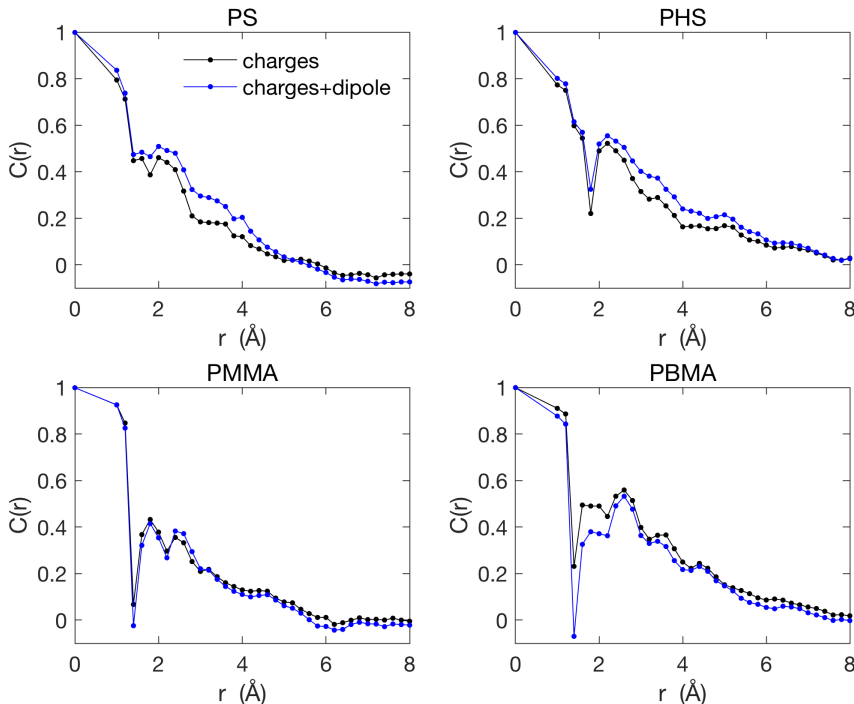

Figure S15: Spatial correlation function of atomic electrostatic potentials, see Equation S1. $C(r)$ decays from 1 (full correlation) at $r = 0$ to 0 (no correlation) a large distance for our samples, approximately following the $1/r$ behavior expected for a collection of randomly oriented dipoles.[16] These data reveal the persistence of significant correlations in the electrostatic potentials over distances comparable to the fragments size, rationalizing the similar spread calculated and measured for core, semi-valence and valence levels. The anomalous fluctuations occurring in the different panels at $r < 2$ Å are due to nonphysical atomic contacts created by the polymer fragmentation and the fragments H capping.
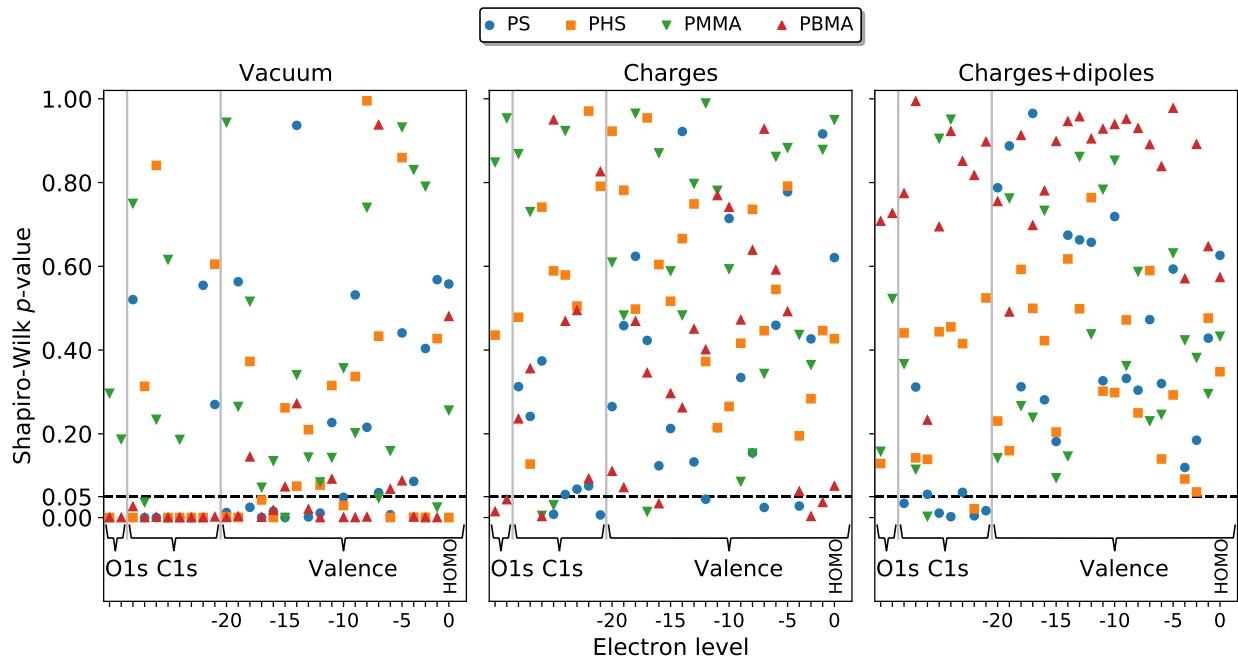
Results of Shapiro–Wilk tests

Figure S16: Results of a Shapiro-Wilk test for normal distribution computed for the 50 calculated binding energies of PS, PHS, PMMA, and PMMA in vacuum (*left*), charges (*center*), and charges+dipoles (*right*) for three types of orbitals, namely O1s (except for PS), C1s, and for the first 20 valence orbitals from HOMO to HOMO−20. Orbitals are ordered by increasing binding energy. The majority of the Shapiro–Wilk p-values lie above 0.05, indicating that the binding energies of the corresponding orbitals can be considered as normally distributed over the sampled fragments and thus justifying the use of Gaussian spectral lines. Using Gaussian peaks for the few orbitals that fail the Shapiro–Wilk test is not expected to significantly affect the total spectral line-shape, especially for the narrow peaks in vacuum, nor change the conclusions of this work.

References

(1) http://scipoly.com/density-of-polymers-by-density/, consulted on 27/06/2023.

(2) Mees, M. J.; Pourtois, G.; Neyts, E. C.; Thijsse, B. J.; Stesmans, A. Uniform-Acceptance Force-Bias Monte Carlo Method With Time Scale To Study Solid-State Diffusion. *Phys. Rev. B* **2012**, *85*, 134301.

(3) Broyden, C. G. The Convergence of a Class of Double-rank Minimization Algorithms 1. General Considerations. *IMA J. Appl. Math.* **1970**, *6*, 76–90.

(4) Kühne, T. D.; Iannuzzi, M.; Ben, M. D.; Rybkin, V. V.; Seewald, P.; Stein, F.; Laino, T.; Khaliullin, R. Z.; Schütt, O.; Schiffmann, F. et al. CP2K: An Electronic Structure and Molecular Dynamics Software Package – Quickstep: Efficient and Accurate Electronic Structure Calculations. *J. Chem. Phys.* **2020**, *152*, 194103.

(5) D'Avino, G.; Muccioli, L.; Zannoni, C.; Beljonne, D.; Soos, Z. G. Electronic Polarization in Organic Crystals: A Comparative Study of Induced Dipoles and Intramolecular Charge Redistribution Schemes. *J. Chem. Theory Comput.* **2014**, *10*, 4959–4971.

(6) TURBOMOLE V7.2 2017, a development of University of Karlsruhe and Forschungszentrum Karlsruhe GmbH, 1989-2007, TURBOMOLE GmbH, since 2007; available from `http://www.turbomole.com`.

(7) Becke, A. D. Density-Functional Exchange-Energy Approximation With Correct Asymptotic Behavior. *Phys. Rev. A* **1988**, *38*, 3098–3100.

(8) Lee, C.; Yang, W.; Parr, R. G. Development of the Colle-Salvetti Correlation-Energy Formula Into a Functional of the Electron Density. *Phys. Rev. B* **1988**, *37*, 785–789.

(9) Becke, A. D. A New Mixing of Hartree–Fock and Local Density-Functional Theories. *J. Chem. Phys.* **1993**, *98*, 1372–1377.

(10) Eichkorn, K.; Treutler, O.; Öhm, H.; Häser, M.; Ahlrichs, R. Auxiliary Basis Sets To Approximate Coulomb Potentials. *Chem. Phys. Lett.* **1995**, *240*, 283–290.

(11) Weigend, F.; Ahlrichs, R. Balanced Basis Sets of Split Valence, Triple Zeta Valence and Quadruple Zeta Valence Quality for H to Rn: Design and Assessment of Accuracy. *Phys. Chem. Chem. Phys.* **2005**, *7*, 3297–3305.

(12) Weigend, F. Accurate Coulomb-Fitting Basis Sets for H to Rn. *Phys. Chem. Chem. Phys.* **2006**, *8*, 1057–1065.

(13) Perdew, J. P.; Burke, K.; Ernzerhof, M. Generalized Gradient Approximation Made Simple. *Phys. Rev. Lett.* **1996**, *77*, 3865–3868.

(14) van Setten, M. J.; Weigend, F.; Evers, F. The GW-Method for Quantum Chemistry Applications: Theory and Implementation. *J. Chem. Theory Comput.* **2013**, *9*, 232–246.

(15) Sajjadian, F. S.; Galleni, L.; Dorney, K. M.; Singh, D. P.; Holzmeier, F.; van Setten, M. J.; Gendt, S. D.; Conard, T. Photoemission Spectroscopy on Photoresist Materials: A Protocol for Analysis of Radiation Sensitive Materials. *J. Vac. Sci. Technol. A* **2023**, *41*.

(16) Novikov, S. V.; Vannikov, A. V. Cluster Structure in the Distribution of the Electrostatic Potential in a Lattice of Randomly Oriented Dipoles. *J. Phys. Chem.* **1995**, *99*, 14573–14576.